

Flat Topological Bands and Eigenstate Criticality in a Quasiperiodic Insulator

Yixing Fu, Justin H. Wilson, and J. H. Pixley

Department of Physics and Astronomy, Center for Materials Theory, Rutgers University, Piscataway, NJ 08854 USA

(Dated: March 22, 2022)

The effects of downfolding a Brillouin zone can open gaps and quench the kinetic energy by flattening bands. Quasiperiodic systems are extreme examples of this process, which leads to new phases and critical eigenstates. We analytically and numerically investigate these effects in a two-dimensional topological insulator with a quasiperiodic potential and discover a complex phase diagram. We study the nature of the resulting eigenstate quantum phase transitions; a quasiperiodic potential can make a trivial insulator topological and induce topological insulator-to-metal phase transitions through a unique universality class distinct from random systems. Additionally, at the transition between trivial and topological insulators, a Dirac semimetal phase is formed that can host a “magic-angle” phase transition due to the quasiperiodic potential. This wealth of critical behavior occurs concomitantly with the quenching of the kinetic energy, resulting in flat topological bands that could serve as a platform to realize the fractional quantum Hall effect without a magnetic field.

The interplay of topology and strong correlations produces a wide range of fascinating phenomena, with the fractional quantum Hall effect [1] serving as the quintessential example. Conventionally, the magnetic field induces topology in the electronic many-body wavefunction; however, Berry curvature of the band structure is sufficient to induce topology in single-particle wavefunctions, which can survive in the presence of interactions (see Ref. 2 for a review). Despite strong numerical evidence of fractional Chern and \mathbb{Z}_2 insulators [3–8], identifying a clear experimental route to the many-body analog of the fractional quantum Hall effect without a magnetic field has remained challenging. A natural direction is to find lattices that host flat topological bands that quench the kinetic energy and promote strong correlations [9–13].

Recent work on twisted graphene heterostructures has opened up new platforms to study strongly correlated physics, including correlated insulators [14], superconductivity [15, 16], and Chern insulators [17–19]. Various proposals for realizing flat topological bands in these systems have followed [20–28]. It was also recently shown in Refs. 29 and 30 that the incommensurate effect of the twist could be emulated by a quasiperiodic potential. Consequently, a class of models, dubbed magic-angle semimetals, show similar phenomena to twisted bilayer graphene (e.g., the formation of minibands and the vanishing Dirac cone velocity) at or near an eigenstate phase transition. Similarly, in order to understand the theory for fractional Chern and \mathbb{Z}_2 insulators in incommensurate systems and how eigenstate criticality can play a role, it is essential to build a simple model to study theoretically and realize experimentally. This notion of flat band engineering with incommensuration can find broad applicability outside twisted heterostructures, including ultra-cold atomic gases and metamaterials (e.g., photonic waveguides, microwave resonators, and topoelectric circuits).

In this letter, we study a minimal model for a two-dimensional topological insulator with a quasiperiodic potential to find a controllable route to create flat topological bands and to induce quantum phase transitions beyond the Landau-Ginzburg paradigm. Using analytic and numeric techniques, we find an intricate phase diagram, as shown in Fig. 1. In particular, quasiperiodicity creates practically flat topological bands near where finite-energy states exhibit criticality. At the transition between topological and trivial insulators, the system realizes a magic-angle semimetal with all of the features previously studied [29]. We further characterize the critical properties of the various eigenstate transitions, understanding them as localization and delocalization transitions in momentum- or real-space bases. While random systems exhibit analogous features [31], these phase transitions represent unique universality classes that, to the best of our knowledge, have not been characterized to date.

Model and approach: To model a two-dimensional topological insulator, we use the Bernevig-Hughes-Zhang (BHZ) lattice model [32] with an additional 2D quasiperiodic potential. The square-lattice Hamiltonian (with sites \mathbf{r}) is block diagonal such that

$$\mathcal{H} = \sum_{\mathbf{r}, \mathbf{r}'} c_{\mathbf{r}'}^\dagger \begin{pmatrix} h_{\mathbf{r}'\mathbf{r}} & 0 \\ 0 & h_{\mathbf{r}'\mathbf{r}}^* \end{pmatrix} c_{\mathbf{r}} + \sum_{\mathbf{r}} c_{\mathbf{r}}^\dagger V(\mathbf{r}) c_{\mathbf{r}}, \quad (1)$$

where $c_{\mathbf{r}}$ are four-component annihilation operators and $V(\mathbf{r}) = W \sum_{\mu=x,y} \cos(Qr_\mu + \phi_\mu)$ is the quasiperiodic potential (QP) with amplitude W , wavevector Q , and random phase ϕ_μ ; $h_{\mathbf{r}'\mathbf{r}}$ is a two-by-two matrix describing one block of the BHZ model (h^* is its complex conjugate). The nonzero elements of h are $h_{\mathbf{r}\mathbf{r}} = (M - 2)\sigma_z$ and $h_{\mathbf{r}, \mathbf{r}+\hat{\mu}} = h_{\mathbf{r}, \mathbf{r}-\hat{\mu}}^\dagger = -\frac{i}{2}t_\mu\sigma_\mu$ for $\mu = x, y$, topological mass M , and hoppings $t_\mu = 1$. Additionally, most analyses are done on this smaller two-by-two matrix since time-reversal symmetry relates each block, and $V(\mathbf{r})$ does not couple blocks. To reduce finite-size effects, we aver-

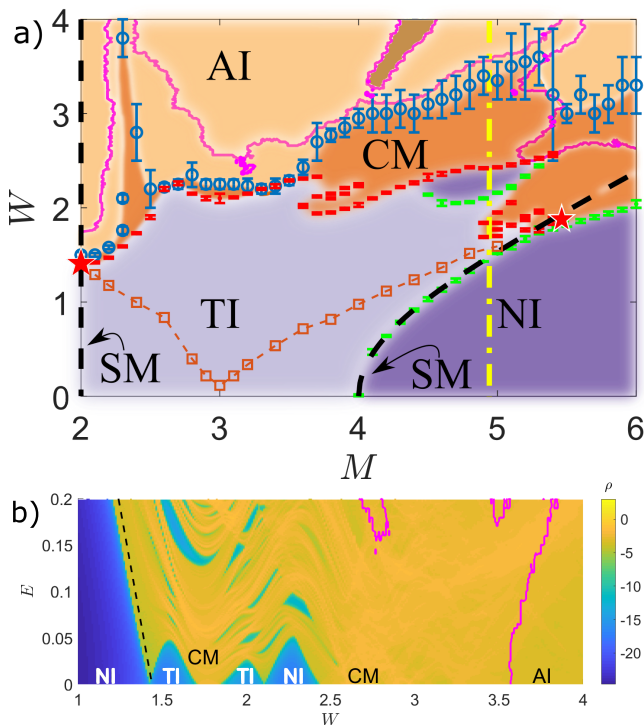


FIG. 1. **Phase Diagram at zero and non-zero energy.** (a) Phase diagram of the Bernevig-Hughes-Zhang model at charge neutrality (i.e., zero energy) with topological mass M and quasiperiodic potential strength W . There are five illustrated phases: topological (TI), normal (NI), and Anderson (AI) insulators, Dirac semimetal (SM), and critical metal (CM). The lines between TI and NI are SMs in addition to the $M = 2$ vertical line. The black dashed lines are the perturbation theory prediction for the SM lines. The green and red data points use the density of states to locate the phase boundaries while the blue circles use transport to determine the boundary from CM to AI. Machine learning on localized and critical eigenstates roughly agrees with these phase boundaries, illustrated with the pink curve. The orange line with square symbols mark the location where the topological bands become flat. (b) A cut of the phase diagram in energy space represented by the yellow line in (a). Notice the multiple phase transitions, all driven by quasiperiodicity (W) in addition to the higher energy metallic nature. The pink curve represents the boundary to machine learned eigenstates that are localized.

age over twisted boundary conditions implemented with $t_\mu \rightarrow t_\mu e^{i\theta_\mu/L}$ for a twist θ_μ in the μ -direction randomly sampled from $[0, 2\pi)$. The model is invariant under $M \rightarrow 4 - M$, so we focus on $M \geq 2$. For $2 < M < 4$, the band structure (i.e. $W = 0$) is topological with a quantized spin Hall effect $\mathcal{Q} = \sigma_{xy}^+ - \sigma_{xy}^-$ where σ_{xy}^\pm are Hall conductivities for the blocks defined by h and h^* respectively. At $M = 2$ [$M = 4$], the model is a Dirac semimetal with Dirac points at $\mathbf{X} = (\pi, 0)$ and $\mathbf{Y} = (0, \pi)$ [$\mathbf{M} = (\pi, \pi)$] that have a velocity $v_0 = t$.

Quasiperiodicity is encoded in Q , which in the thermodynamic limit we define as $Q/(2\pi) = (2/(\sqrt{5} + 1))^2$.

For simulations, we take rational approximates such that $Q \approx Q_L = 2\pi F_{n-2}/F_n$, where F_n is the n th Fibonacci number, and the system size is $L = F_n$. In the supplement, we consider other values of Q .

In the following, we investigate eigenstates, eigenvalues, and the transport properties of the system. To compute the transport and density of states (DOS), we use the kernel polynomial method (KPM) [33]. The KPM utilizes a Chebyshev expansion truncated at an integer N_c , which controls the energy resolution. To evaluate the conductivity tensor we use the Kubo formula [34]

$$\sigma_{\alpha\beta} = \frac{2e^2\hbar}{L^2} \int f(E) dE \text{Im Tr} \left[v_\alpha \frac{dG^-}{d\epsilon} v_\beta \delta(E - H) \right] \quad (2)$$

where $f(E) = [e^{\beta(E-\mu)} + 1]^{-1}$ is the Fermi function at inverse temperature β and chemical potential μ , v_α is the velocity operator, G^- is the retarded Green function, and $[\cdot \cdot \cdot]$ denotes an average over phases in the QP (ϕ_μ) and twists (θ_μ) in the boundary condition; for numerical data, we average over 200 samples. In contrast to disordered systems, band gaps are cleanly identifiable with the DOS

$$\rho(E) = \frac{1}{2L^2} \left[\sum_i \delta(E - E_i) \right] \quad (3)$$

where E_i denotes the energy eigenvalues.

To probe wavefunctions, we compute the inverse participation ratios (IPRs) in real and momentum space. The IPR in a basis indexed by α is

$$\mathcal{I}_\alpha(E) = \sum_{\alpha} [|\langle \alpha | \psi_E \rangle|^4] \quad (4)$$

where the wavefunctions are normalized to unity and in the momentum space ($\alpha = \mathbf{k}$) or real space ($\alpha = \mathbf{r}$) basis. We use exact diagonalization on small system sizes and Lanczos for larger system sizes to compute $\langle \alpha | \psi_E \rangle$. For systems localized in basis α , the IPR is L -independent; for delocalized systems, it goes like $\mathcal{I}_\alpha \sim 1/L^2$. At a localization transition [35, 36] $\mathcal{I}_\alpha \sim 1/L^\gamma$ where γ is related to the fractal dimension (d_2) and $0 < \gamma < 2$.

Lastly, due to the great deal of structure in the phase diagram we use machine learning [37] on the eigenstates to identify different phases in the model. A neural network model is trained using a subset of manually labelled data on the wavefunctions as extended, critical, or localized. The neural net model generalizes the identification to any combination of parameters (W , M , and E) to efficiently calculate the phase boundary and mobility edge (to Anderson localized phases) with a high resolution in parameter space. We validate this approach by comparing with the conductivity and IPR to determine a comprehensive phase diagram.

Phase Diagram: Using analytic and numeric techniques, we obtain the phase diagrams shown in Fig. 1. There are principally five phases pictured: topological insulator (TI), normal insulator (NI), critical metal (CM),

Anderson insulator (AI), and lines of Dirac semimetals (SM) between TI and NI phases. Both band-insulating and SM phases are stable to weak quasiperiodicity. Finite band gaps and quantized (zero) spin Hall conductivity describe the TI (NI) phase. Low-energy scaling of the DOS captures the SM phases ($\rho(E) \sim \tilde{v}^{-2}|E|$ for a 2D Dirac cone with renormalized velocity \tilde{v}). The AI phase has a finite DOS but zero conductivity and localized wave functions (real space IPR that is L -independent). We further use a machine learning algorithm that identifies delocalized, localized, and critical eigenstates to supplement other measures. The structure revealed is Q -dependent [37] and reminiscent of other studies of insulating phases perturbed by quasiperiodicity [38].

Upon increasing W , we usually traverse the phases TI/NI \rightarrow CM \rightarrow AI. However, more complicated cuts are possible as shown in Fig. 1(b); simply increasing W leads to the phases NI \rightarrow SM \rightarrow TI \rightarrow CM \rightarrow TI \rightarrow SM \rightarrow NI \rightarrow CM \rightarrow AI along with bands and mobility edges shown. We see that quasiperiodicity can drive trivial phases topological (for $4 < M \lesssim 5.0$) and into-and-out-of metallic and topological phases at zero-energy. Intriguingly, near the dashed orange line (with square symbols) in Fig. 1(a) higher-energy bands (some with nonzero topological index) flatten, the effective mass effectively diverges ($\sim 10^5$ increase), and the eigenstates appear critical as measured by the IPRs.

The physics on the SM lines emanating from $M = 2$ or $M = 4$ at $W = 0$ agrees with the universal features found in Ref. 29 and reveals magic-angle transitions marked by red stars in Fig. 1(a). Concentrating on $M = 2$, the semimetal is stable with a velocity (calculated from the DOS) that vanishes like $\tilde{v} \sim (W_c(M = 2) - W)^{\beta/2}$ where $W_c(M = 2) = 1.42 \pm 0.02$ and $\beta = 2 \pm 0.3$, which is close to the universal value $\beta \approx 2$ obtained in other models and symmetry classes [29, 30]. This is demonstrated in Fig. 2(a) where \tilde{v} vanishes when $\rho(0)$ rises. Additionally, the wave functions are localized in momentum space when $W < W_c(M = 2)$, and delocalized in momentum space when $W > W_c(M = 2)$ (as indicated in Fig. 2(b) by \mathcal{I}_k being L -independent and $\mathcal{I}_k \sim 1/L^2$, respectively). When the wave function is localizing (indicated by real space IPR) and the resistivity is increasing with L and N_c , there is a localization transition $W_A(M = 2) = 1.50 \pm 0.03$, indicating a small but finite CM phase.

From the neural net model we have determined an additional measure of the Anderson localization transition, shown as the magenta line in Fig. 1(a). In the current Hamiltonian, the critical eigenstates can appear very close to being localized and therefore are not straightforward to diagnose with the IPR and conductivity alone. Thus, we use machine learning to provide a more conservative measure of the Anderson localized phase, which in certain regimes matches the IPR and conductivity, but in the more non-trivial regimes of the phase diagram ex-

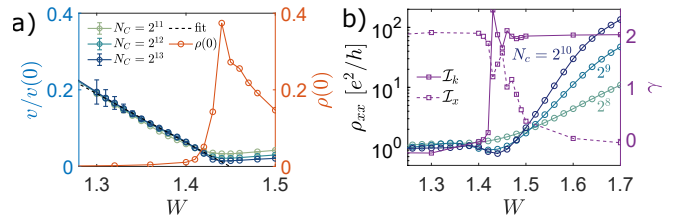


FIG. 2. **The magic-angle transition for the semimetal line $M = 2$.** (a) Renormalized velocity $v/v(0)$ and the resulting finite density of states $\rho(0)$ at the transition, calculated with system size $L = 144$ and Chebyshev cutoff $N_c = 2^{15}$. (b) These plots indicate the appearance of a critical metallic phase $1.4 \lesssim W \lesssim 1.5$ inferred from both the resistivity ρ_{xx} and the scaling of the momentum- and real-space IPRs. The L -dependence of the IPRs is fitted from $L = 89$, $L = 144$, and $L = 233$ to a power law form $\mathcal{I}_\alpha \sim 1/L^{\gamma_\alpha}$, and γ_α is shown as the right vertical axis.

tends to larger values of W .

Perturbation theory and NI-to-TI transition: For smaller values of W , we use perturbation theory to map out the phase diagram and estimate the location of the NI-to-TI and SM-to-CM transitions.

To perform perturbation theory on the BHZ Hamiltonian $h_0(\mathbf{k})$, we use Dyson's equation $G(\mathbf{k}, \omega)^{-1} = \omega - h_0(\mathbf{k}) - \Sigma(\mathbf{k}, \omega)$ to evaluate the self-energy $\Sigma(\mathbf{k}, \omega)$ by treating $V(\mathbf{r})$ perturbatively [37]. To illustrate, near $M = 4$ we take a single two-by-two block of the full Hamiltonian and expand it in the low-energy limit at $W = 0$ (near the Dirac cone at $\mathbf{k} = \mathbf{M}$) so that $h_0(\mathbf{M} + \mathbf{q}) = v\mathbf{q} \cdot \boldsymbol{\sigma} + (M - 4)\sigma_z$. Putting the resulting Green function in the form $G(\mathbf{M} + \mathbf{q}, \omega) = Z[\omega - \tilde{v}\mathbf{q} \cdot \boldsymbol{\sigma} - \tilde{M}\sigma_z]^{-1}$ defines the quasiparticle residue Z , renormalized velocity \tilde{v} , and topological mass \tilde{M} . In this regime (for $M = 4$), we obtain up to second order for \tilde{M}

$$\tilde{M} - 4 = \frac{\left[(M - 4) + W^2 \frac{(4 - M) + (\cos Q - 1)}{(4 - M)^2 + 2(3 - M)(\cos Q - 1)} \right]}{1 + W^2 / ((4 - M)^2 + 2(3 - M)(\cos Q - 1))}. \quad (5)$$

where the denominator is Z . By solving for $\tilde{M} = 4$, we obtain the phase boundary between distinct insulating phases, as illustrated by the black dotted line in Fig. 1(a) (at fourth-order in W), which is in excellent agreement with the numerics. The curvature to this line demonstrates that quasiperiodicity can drive a topological phase transition NI-to-TI, which is the deterministic analog of the disordered topological Anderson insulator [31]. Note that for $M = 2$ the line $\tilde{M} = 0$ is completely vertical. Using numerics to access higher M and W , we find for $M \gtrsim 5.4$ the NI transitions directly into the CM phase. The magic-angle transition (i.e. SM-to-CM) is obtained by solving for when $\tilde{v} \rightarrow 0$ on the line $\tilde{M} = 0$.

To quantify band flatness, we find the dispersion relation from the pole of the Green function $E_{\text{eff}}(\mathbf{q}) = \pm(\tilde{M} + q^2/2m^*)$ with effective mass $m^* = \tilde{M}/(2\tilde{v}^2)$. At

fourth-order we find that $m^* \sim 10^5(1/t)$ at $W = 3t$, our first indication that the QP is flattening the topological bands; our numerics show that this effect is even more drastic.

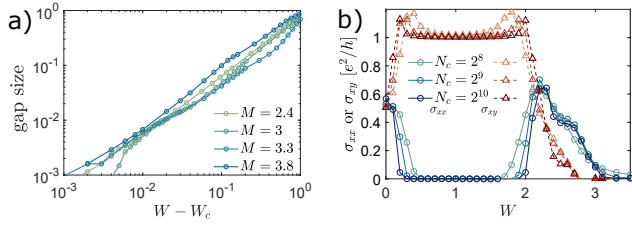


FIG. 3. Demonstration of the TI to CM transition. (a) By tracking the density of states, we see the gap closes when the longitudinal conductivity becomes finite and the gap vanishes as a power law $\Delta = (W_c(M) - W)^{\nu z}$ with $\nu z \approx 1$ at the TI-to-CM transition across each value of M . (b) Shows the conductivity as a function of quasiperiodic strength W for $M = 4.0$. The Hall conductivity σ_{xy} saturates to a finite value in the TI phase, but for $2 \lesssim W \lesssim 3$ the longitudinal conductivity becomes finite and the Hall part is suppressed. The system is localized when $W \gtrsim 3$. Note that the feature near $W = 0$ is due to $M = 4$ being a SM.

TI-to-CM transition: We use numerics to capture the full, nonperturbative transition to the CM phase. Generically, we denote as $W_c(M)$ the phase transition into the CM phase. Near the transition, we find that the gap closes as $\Delta \sim |W - W_c(M)|^{\nu z}$ and $\nu z \approx 1$ for each M value we have considered (ν is the correlation length exponent and z is the dynamical exponent), see Fig. 3(a). These exponents indicate a unique universality class driven by quasiperiodicity distinct from random systems, where $\nu \sim 2.7$ has been estimated in the case of random disorder [39] and $\nu \sim 5$ for random impurities [40], and they both have $z = d$ [36].

As the gap closes at $W_c(M)$, the conductivity at $E = 0$ becomes finite, and the Hall conductivity is no longer quantized, indicating the onset of the CM phase. As seen in Fig. 3(b), the Hall conductivity drops, and σ_{xx} peaks at the transition, remaining finite for the duration of the CM. For larger values of W , we find a transition into an Anderson insulating phase [36, 41] with exponentially localized wavefunctions in real space and a vanishing σ_{xx} . Additionally, as Fig. 1(b) shows, we can have a more complicated structure for various sequences of transitions as well.

Criticality and flat topological bands: At small W , the gap *increases* for some values of M , as seen in Fig. 4(a) (and as indicated by perturbation theory for \bar{M} [37]). For larger W , the gap begins decreasing (indicated roughly by the orange dashed line with square symbols in Fig. 1(a)). When the gap begins decreasing, several phenomena occur, seen in Fig. 4 for the cut $M = 4.0$. We track the effective mass m^* and find that it increases almost over four orders of magnitude [Fig. 4(a)], indicat-

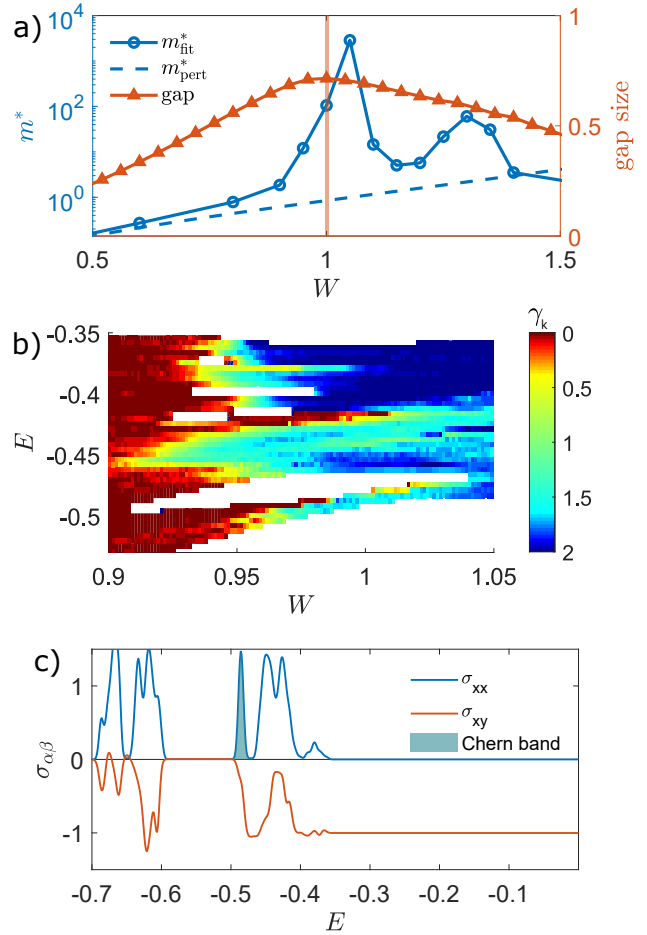


FIG. 4. Flat Chern bands and eigenstate criticality. (a) The effective mass of the lowest band as a function of W and gap size. Notice that the gap begins to decrease when the effective mass calculated numerically exceeds its perturbative value by $\sim 10^3$. (b) Color plot of the momentum-space IPR scaling at these higher energies. Notice that around $W \sim 0.95$ many parts of the spectrum start becoming delocalized in momentum space. At low energies the states become completely delocalized (and even localize in real space), while at higher energies $\mathcal{I}_k \sim L^{-\gamma_k}$ for $0 < \gamma_k < 2$ indicating critical eigenstates and the value of γ_k is given by the color. The lowest energy band (and flattest) is actually the Chern band. (c) A demonstration of the flat Chern band for $W = 1$. From figure (b) we know that it is made up of critical eigenstates, and yet the Chern number (as indicated by σ_{xy}) jumps abruptly across the band.

ing the onset of flat bands and the breakdown of perturbation theory. Additionally, the states in the bands become critical, as measured by the IPR in momentum and position space ($1/\mathcal{I}_\alpha \approx L^{\gamma_\alpha}$ for $0 < \gamma_\alpha < 2$ to delocalized in both bases ($\alpha = x, k$) [Fig. 4(b)]. Right after the states begin exhibiting critical behavior, we can isolate flat topological bands as in Fig. 4(c) by studying the change in σ_{xy} across a band (we also see edge states[37]). These “bands” can be thought of as a collection of states

for which quasiperiodicity still causes level repulsion, but at smaller energy scales. Intuitively, as quasiperiodicity downfolds the Brillouin zone, some states get pushed up (the topological) and others down (trivial states); as they pass through each other, they hybridize and split becoming critical while simultaneously flattening.

At other points along the dashed line in Fig. 1, it is less clear how to separate the topological band from the zoo of nearby trivial bands, but other instances of flat topological bands are not hard to isolate. Remarkably, flat bands with eigenstate criticality occurring in tandem is very similar to magic-angle semimetals [29].

Conclusion— In a simple 2D TI, we demonstrated that the inclusion of quasiperiodicity induces flat bands, eigenstate criticality, and a phase diagram full of structure. This was achieved by generalizing a quasiperiodic perturbative analysis to TIs and extensive numerics (using KPM, exact diagonalization, Lanczos methods, and machine learning). The eigenstates go through several Anderson-like transitions (delocalizing in momentum space before localizing in real space), which leads to critical eigenstates in a metallic phase. Meanwhile, we see the onset of flat topological bands within the TI phase concomitant with critical high energy eigenstates. Just as Dirac semimetals with quasiperiodicity are analogous to twisted bilayer graphene, TIs with quasiperiodicity achieve flat topological bands similar to twisted heterostructures. This identification allows for cold atom labs and metamaterial labs (both of which have already realized 2D TIs [42–45]) to emulate similar physics.

We thank Yafis Barlas and Elio König for useful discussions. The authors acknowledge the following research computing resources that have contributed to the results reported here: the Open Science Grid [46, 47], which is supported by the National Science Foundation award 1148698, and the U.S. Department of Energy’s Office of Science, the Beowulf cluster at the Department of Physics and Astronomy of Rutgers University; and the Office of Advanced Research Computing (OARC) at Rutgers, The State University of New Jersey (<http://oarc.rutgers.edu>), for providing access to the Amarel cluster.

[1] H. L. Stormer, D. C. Tsui, and A. C. Gossard, *Reviews of Modern Physics* **71**, S298 (1999).
 [2] J. Maciejko and G. A. Fiete, *Nature Physics* **11**, 385 (2015).
 [3] N. Regnault and B. A. Bernevig, *Physical Review X* **1**, 021014 (2011).
 [4] Z. Liu, E. J. Bergholtz, H. Fan, and A. M. Läuchli, *Physical review letters* **109**, 186805 (2012).
 [5] F. Harper, S. H. Simon, and R. Roy, *Physical Review B* **90**, 075104 (2014).
 [6] M. A. Bandres, M. C. Rechtsman, and M. Segev, *Physical Review X* **6**, 011016 (2016).
 [7] J. Maciejko, X.-L. Qi, A. Karch, and S.-C. Zhang, *Phys-*

ical review letters **105**, 246809 (2010).
 [8] B. Swingle, M. Barkeshli, J. McGreevy, and T. Senthil, *Physical Review B* **83**, 195139 (2011).
 [9] E. J. Bergholtz and Z. Liu, *International Journal of Modern Physics B* **27**, 1330017 (2013).
 [10] S. A. Parameswaran, R. Roy, and S. L. Sondhi, arXiv preprint arXiv:1302.6606 (2013).
 [11] Y.-F. Wang, H. Yao, C.-D. Gong, and D. Sheng, *Physical Review B* **86**, 201101 (2012).
 [12] S. Yang, Z.-C. Gu, K. Sun, and S. D. Sarma, *Physical Review B* **86**, 241112 (2012).
 [13] T. T. Heikkilä, N. B. Kopnin, and G. E. Volovik, *JETP letters* **94**, 233 (2011).
 [14] Y. Cao, V. Fatemi, A. Demir, S. Fang, S. L. Tomarken, J. Y. Luo, J. D. Sanchez-Yamagishi, K. Watanabe, T. Taniguchi, E. Kaxiras, *et al.*, *Nature* **556**, 80 (2018).
 [15] Y. Cao, V. Fatemi, S. Fang, K. Watanabe, T. Taniguchi, E. Kaxiras, and P. Jarillo-Herrero, *Nature* **556**, 43 (2018).
 [16] M. Yankowitz, S. Chen, H. Polshyn, Y. Zhang, K. Watanabe, T. Taniguchi, D. Graf, A. F. Young, and C. R. Dean, *Science* **363**, 1059 (2019).
 [17] E. M. Spanton, A. A. Zibrov, H. Zhou, T. Taniguchi, K. Watanabe, M. P. Zaletel, and A. F. Young, *Science* **360**, 62 (2018).
 [18] C. Knapp, E. M. Spanton, A. F. Young, C. Nayak, and M. P. Zaletel, *Physical Review B* **99**, 081114 (2019).
 [19] A. L. Sharpe, E. J. Fox, A. W. Barnard, J. Finney, K. Watanabe, T. Taniguchi, M. Kastner, and D. Goldhaber-Gordon, *Science* **365**, 605 (2019).
 [20] Y.-H. Zhang, D. Mao, Y. Cao, P. Jarillo-Herrero, and T. Senthil, *Physical Review B* **99**, 075127 (2019).
 [21] B. L. Chittari, G. Chen, Y. Zhang, F. Wang, and J. Jung, *Physical review letters* **122**, 016401 (2019).
 [22] F. Wu, *Physical Review B* **99**, 195114 (2019).
 [23] T. M. Wolf, O. Zilberberg, I. Levkivskiy, and G. Blatter, *Physical Review B* **98**, 125408 (2018).
 [24] Q. Tong, H. Yu, Q. Zhu, Y. Wang, X. Xu, and W. Yao, *Nature Physics* **13**, 356 (2017).
 [25] P. San-Jose, A. Gutiérrez-Rubio, M. Sturla, and F. Guinea, *Physical Review B* **90**, 115152 (2014).
 [26] B. Lian, Z. Liu, Y. Zhang, and J. Wang, arXiv preprint arXiv:1908.02581 (2019).
 [27] P. J. Ledwith, G. Tarnopolsky, E. Khalaf, and A. Vishwanath, arXiv preprint arXiv:1912.09634 (2019).
 [28] Z. Song, Z. Wang, W. Shi, G. Li, C. Fang, and B. A. Bernevig, *Physical review letters* **123**, 036401 (2019).
 [29] Y. Fu, E. König, J. Wilson, Y.-Z. Chou, and J. Pixley, arXiv preprint arXiv:1809.04604 (2018).
 [30] Y.-Z. Chou, Y. Fu, J. H. Wilson, E. König, and J. Pixley, arXiv preprint arXiv:1908.09837 (2019).
 [31] C. Groth, M. Wimmer, A. Akhmerov, J. Tworzydło, and C. Beenakker, *Physical review letters* **103**, 196805 (2009).
 [32] B. A. Bernevig, T. L. Hughes, and S.-C. Zhang, *Science* **314**, 1757 (2006).
 [33] A. Weiße, G. Wellein, A. Alvermann, and H. Fehske, *Reviews of modern physics* **78**, 275 (2006).
 [34] J. H. García, L. Covaci, and T. G. Rappoport, *Physical review letters* **114**, 116602 (2015).
 [35] A. D. Mirlin, *Physics Reports* **326**, 259 (2000).
 [36] F. Evers and A. D. Mirlin, *Reviews of Modern Physics* **80**, 1355 (2008).
 [37] Supplementary Materials to this publication.
 [38] G. Roux, T. Barthel, I. McCulloch, C. Kollath,

- U. Schollwöck, and T. Giamarchi, *Physical Review A* **78**, 023628 (2008).
- [39] A. Yamakage, K. Nomura, K.-I. Imura, and Y. Kuramoto, *Physical Review B* **87**, 205141 (2013).
- [40] C.-Z. Chen, H. Liu, H. Jiang, Q.-f. Sun, Z. Wang, and X. Xie, *Physical Review B* **91**, 214202 (2015).
- [41] E. Abrahams, P. Anderson, D. Licciardello, and T. Ramakrishnan, *Physical Review Letters* **42**, 673 (1979).
- [42] C. W. Peterson, W. A. Benalcazar, T. L. Hughes, and G. Bahl, *Nature* **555**, 346 (2018).
- [43] R. Süsstrunk and S. D. Huber, *Science* **349**, 47 (2015).
- [44] E. Lustig, S. Weimann, Y. Plotnik, Y. Lumer, M. A. Bandres, A. Szameit, and M. Segev, *Nature* **567**, 356 (2019).
- [45] C. J. Kennedy, G. A. Siviloglou, H. Miyake, W. C. Burton, and W. Ketterle, *Physical review letters* **111**, 225301 (2013).
- [46] R. Pordes, D. Petravick, B. Kramer, D. Olson, M. Livny, A. Roy, P. Avery, K. Blackburn, T. Wenaus, F. Würthwein, I. Foster, R. Gardner, M. Wilde, A. Blatecky, J. McGee, and R. Quick, in *J. Phys. Conf. Ser.*, **78**, Vol. 78 (2007) p. 012057.
- [47] I. Sfiligoi, D. C. Bradley, B. Holzman, P. Mhashilkar, S. Padhi, and F. Wurthwein, in *2009 WRI World Congress on Computer Science and Information Engineering*, **2**, Vol. 2 (2009) pp. 428–432.

Supplement to “Flat Topological Bands and Eigenstate Criticality in a Quasiperiodic Insulator”

Yixing Fu, Justin H. Wilson, and J. H. Pixley

Department of Physics and Astronomy, Center for Materials Theory, Rutgers University, Piscataway, NJ 08854 USA

(Dated: February 28, 2020)

In the following supplemental material we provide details about the machine learning algorithm we have used, the perturbation theory at second and fourth order in the potential, as well as additional numerical results to support our findings in the main text.

CONTENTS

I. Additional properties of the phase diagram	1
A. Dependence on the quasiperiodic wavevector Q	1
B. Chemical Potential dependence of σ_{xy}	1
II. Machine Learning the localization transition	2
III. Perturbation theory at second and fourth order	4
IV. Finite size effects	6
A. Density of states and conductivity	6
B. Inverse Participation Ratio	7
V. Extracting the spectral gap	7
A. Critical Exponents at the topological insulator to metal phase transition	8
B. Gapsizes and IPR	8
VI. Dispersion relation and effective mass	9
A. Edge states	9
References	9

I. ADDITIONAL PROPERTIES OF THE PHASE DIAGRAM

A. Dependence on the quasiperiodic wavevector Q

In the main text we have focused on a quasiperiodic wavevector $Q = 2\pi F_{n-2}/F_n$ and linear system size $L = F_n$, where F_n is the n th Fibonacci number. The structure of the phase diagram is strongly dependent on the incommensurate value of Q chosen. Here, we show the zero energy density of states that probes insulating, semimetallic, and metallic parts of the phase diagram (but cannot discern between delocalized and localized wavefunctions) in Fig. S1 for $Q = F_{n-3}/F_n$ (a) and $Q = F_{n-4}/F_n$ (b). With these smaller values of Q , the semimetal-to-metal magic-angle transition along $M = 2$ happens for smaller values of W . Qualitatively, this behavior is captured by the perturbation theory near $W = 0$, where it shows the Dirac cone velocity v is renormalized more strongly for smaller values of Q . However, for even smaller Q , higher order perturbation theory is required to see the velocity renormalizing down to 0. On the other hand, the phase boundary rooted from $M = 4$ and $W = 0$ along the NI-to-TI phase boundary can be predicted well by the perturbation theory (shown as a red line in Fig. S1).

B. Chemical Potential dependence of σ_{xy}

The Chern number is directly determined by the Hall conductivity σ_{xy} . While we use $\rho(0)$ to accurately locate phase boundaries, the numerical calculation of σ_{xy} at large system sizes has more computational complexity. However, σ_{xy} can be used to distinguish trivial and topological states and locate where the Chern bands are in energy. Here,

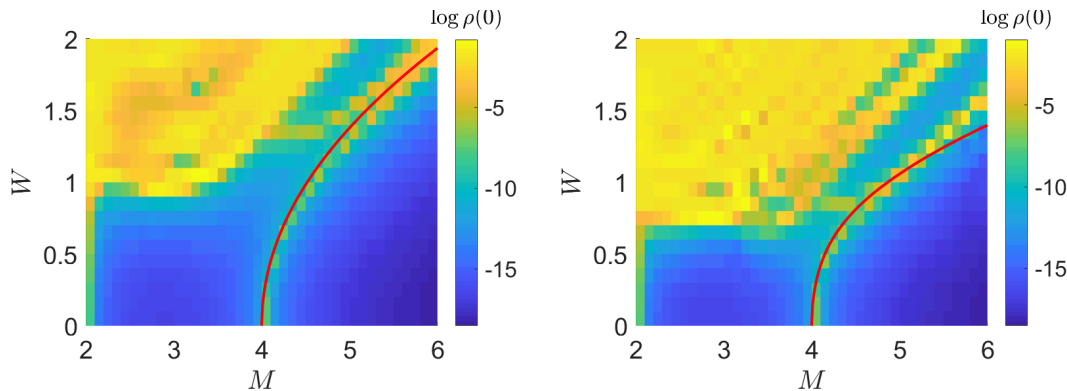


FIG. S1. **Phase diagram determined from density of states at $E_F = 0$ for $Q = F_{n-3}/F_n$ and $Q = F_{n-4}/F_n$.** The red line shown is the result of fourth order perturbation theory used to determine the location of the NI-to-TI transition from the vanishing of the renormalized topological mass \tilde{M} . The perturbative result agrees well with the numerics up to $W \approx 1$.

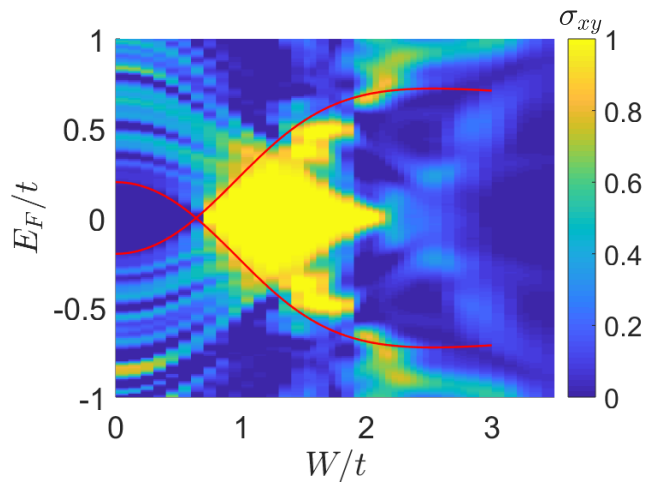


FIG. S2. **Finite energy topological phase diagram.** The Hall conductivity σ_{xy} at various Fermi energies E_F and quasiperiodicity W . The red lines are the perturbation theory prediction of gap size.

we show an example of a color plot of σ_{xy} at a fixed $M = 4.2$ and varying the Fermi energy E_F and disorder strength W , see Fig. S2. The emergence of a topological phase after the collapse of the (lowest energy) trivial band gap can be seen clearly. In addition, our perturbative result (shown as the red lines) is in excellent agreement with the numerics in locating these phase boundaries for $0 \leq W \lesssim 2$.

II. MACHINE LEARNING THE LOCALIZATION TRANSITION

In the present model, we found it challenging to pinpoint the Anderson localization transition using conductivity and the inverse participation ratio due to a large number of critical states that can appear localized by some metrics but not others. Therefore, we have supplemented this analysis with a machine learning classification of the single particle wavefunctions.

Machine learning is a class of methods where a non-specialized program can be used to perform a specific task when supplied with an abundance of data. Many machine learning techniques have been applied to various aspects of physics^{S1-S3}. In this work we used Convolutionary Neural Networks (CNN) to distinguish whether a wave function is localized or extended. We train the neural network on a set of wave functions whose localized nature can be easily and unambiguously determined. Such a neural network automatically applies to all other points in the phase diagram, determining the phase boundaries efficiently and objectively.

A neural network consists of a massive number of nonlinear functions and linear transformations, usually as several “layers,” to replicate any task that distills information from data. Practically, such a combination can be tuned to fit

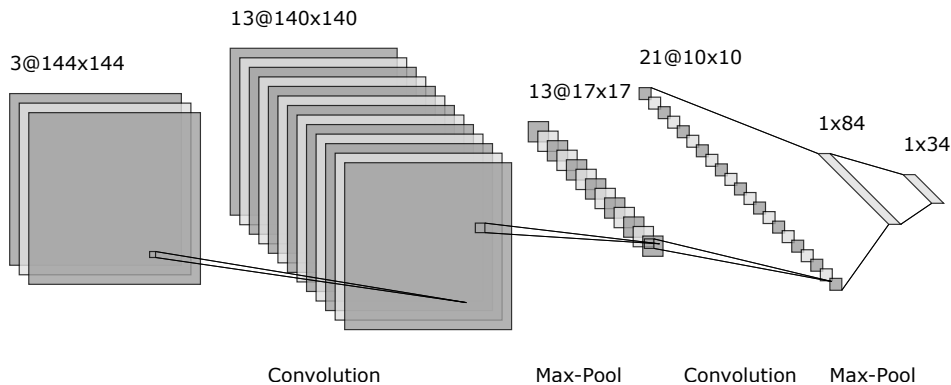


FIG. S3. **Schematic diagram of the neural network structure used for localization detection.** For convolution layers, we apply a convolution operation over a small window to get a data point in the next layer. Max-Pool layer simply takes the maximum of each window to reduce the model size. We also add batch-normalization and dropout layers before and after Max-Pool, but they are not shown here as they do not alter the overall architecture.

any mapping. Hence, as long as a concrete definition of the task to be executed is available, we can use labelled data as an example to tune the neural network until it replicates the task. Such a process is called “training,” and can be calculated efficiently using modern computers.

In the present context, the problem that we want the neural network to solve is to distinguish localized wavefunctions from extended ones. This task can be thought of as a mapping from the space of all wavefunctions to a binary result of localized or extended. Using a set of wavefunctions labelled in advance, we can train the neural network to capture the relation between wavefunction data and the prediction of a localized phase. Once the training is finished, we can use the neural network model to classify a much larger dataset of wavefunctions, and map out a detailed phase diagram.

One crucial but more technical component of deep learning is the choice of the form and organization (i.e., “architecture”) of the nonlinear functions used to fit^{S4,S5}. In this work, we use a simple version of CNN. The wavefunction classification task is somewhat analogous to figuring out whether the image includes a dog or cat, which is a classical application of CNN. The CNN architecture makes use of a convolution operation prior to applying the nonlinear functions. The convolution operations effectively scrambles but preserves the information at various locations of the input data, and hence makes the model “translational invariant”, i.e. the location of the feature does not affect the output. Such translational invariance allows the neural net model to treat critical and/or localized structures at different locations in the same way.

The neural network methods of machine learning usually suffer from over-fitting that harms the predictive power of the model. Simple and conventional methods against over-fitting including adding regularization terms, use of drop-off layers^{S6} and so on. These methods are practically efficient and sufficient for our purpose.

A summary of the architecture we have used with a convolutionary neural network and drop-off layers is shown in Fig. S3. We experimented with a few different hyper parameters of the CNN architectures, and the model yields similar results. Hence the neural net model we have used is not a result of fine tuning. The robustness across different setups is likely because the localization feature is prominent and less ambiguous as opposed to typical computer vision tasks.

The training set is constructed in two different ways:

1. We look at the images to judge whether each wavefunction is clearly localized or not. The cases in which we are unsure are discarded from the training set. To minimize the affect of systematic bias caused in labelling the training set, we go through wavefunctions at several runs where each set is drawn randomly from the entire collection of wavefunctions and shuffled. Hence, the mislabelling can be considered as a random variation that is independent from the features that do not affect decision boundaries.
2. We choose $W > 6$ for localized wavefunction examples, and sample $W = 0$ at various values of M for extended wavefunctions.

The training set of method 2 does not include any of the critical wavefunctions in the CM phase. As a result, the CNN model identifies the critical phase as localized, producing a phase boundary in line with SM/TI to CM transition. This result can also be replicated using the training set from method 1 if we only include extended and fully localized wavefunctions. However, with method 1 we can instead label a dataset such that the non-localized

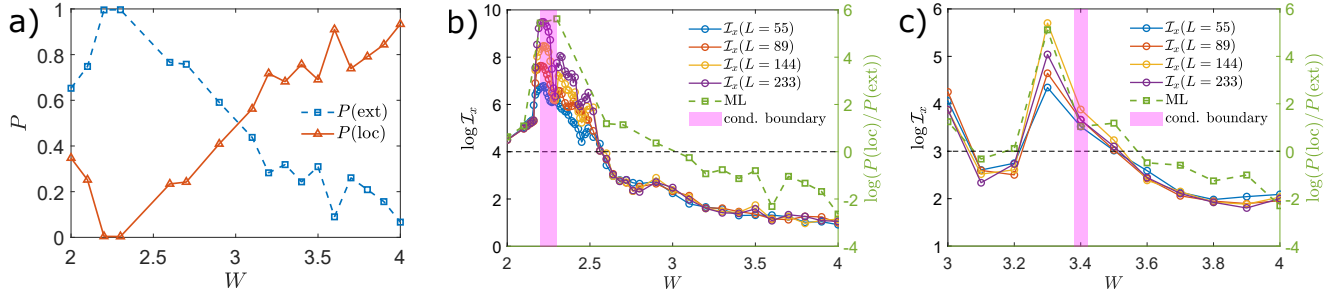


FIG. S4. **Comparing the IPR with the machine learning outcome.** (a) Shows an example of the neural network output for $M = 2.7$, given as the probability of a state being localized [$P(\text{loc})$] or extended [$P(\text{ext})$]. The summarized results are shown for $M = 2.7$ (b) and $M = 4.9$ (c), with comparison against KPM and IPR results. The difference between the two probabilities measures how confidently the model can distinguish localized or extended. Also shown in the figure with the magenta strips is the phase boundary determined by the conductivity, which indicates a transition near $W = 2.25$ for $M = 2.7$, and $W = 3.4$ for $M = 4.9$. Although the three different methods match quite well for $M = 4.9$, for $M = 2.7$ the IPR shows strongly critical behavior up until $W = 2.5$, well after the conductivity appears to vanish. Such critical behavior is detected by the neural net model. For W between 2.3 and 2.5 the IPR shows a strong L dependence and the neural net model predicts an extended phase with high confidence. For a range of W larger than 2.5, the IPR shows a weak L dependence across different system sizes, while in the neural net model $P(\text{loc})$ and $P(\text{ext})$ are quite close to each other.

label *includes* critical wavefunctions to provide an interesting complement to the KPM results and is hence included in the main results of Figure 1.

The phase boundary obtained from machine learning between localized and non-localized wavefunctions roughly traces the CM-AI phase boundary provided by the conductivity computed with the KPM for M between 3.8 and 5.4, but it provides a slightly different boundary elsewhere. For $M < 3.8$, the machine learning result labels regions as critical that have a conductivity that looks localized (i.e. σ_{xx} is vanishing with increasing N_c). We further investigate the nature of this region using the inverse participation ratio (IPR) in real and momentum space bases, see Fig. S4. The IPR in this region shows critical behavior that transits into a localized phase at a point that is hard to accurately determine. The machine learning result provides a conservative estimate of where the criticality ends and localization sets in.

In summary, our use of the machine learning method in the present context is to provide an additional measure of the non-trivial phase boundaries that have a lot of structure. We then use conventional methods (conductivity and the IPR) to validate the physical nature of the phase boundaries.

III. PERTURBATION THEORY AT SECOND AND FOURTH ORDER

In this section, we provide additional details on the perturbation theory at second and fourth order that correctly captures the renormalization of the topological mass (to describe phase transitions in and out of the TI) and the velocity in the SM phase.

We begin by considering the single-particle Green function

$$\hat{G}_0(\omega) = [\omega - h_0(\omega)]^{-1}, \quad \hat{G}(\omega) = [\omega - h_0(\omega) + V]^{-1} \quad (\text{S1})$$

and use Dyson's equation

$$G(\mathbf{k}, \omega)^{-1} = \omega - h_0(\mathbf{k}) - \Sigma(\mathbf{k}, \omega) \quad (\text{S2})$$

where $\Sigma(\mathbf{k}, \omega)$ is the self-energy at momentum \mathbf{k} including all $G_0(\mathbf{k}, \omega)$ irreducible diagrams. Close to the SM phase near $M = M_1 \equiv 2$ or $M = M_2 \equiv 4$, we express the Hamiltonian in the low-energy limit around the corresponding Dirac node \mathbf{K} as $h_0(\mathbf{K} + \mathbf{q}) = v\mathbf{q} \cdot \boldsymbol{\sigma} + (M - M_i)\sigma_z$ and similarly expand the self-energy to obtain $\Sigma(\mathbf{k} = \mathbf{K} + \mathbf{q}, \omega) = \omega \Sigma_E \sigma_0 + \Sigma_p \mathbf{q} \cdot \boldsymbol{\sigma} + \Sigma_z \sigma_z$ (where σ_0 is the 2-by-2 identity matrix and the $\sigma_{x,y,z}$ are the Pauli matrices). We define the quasiparticle residue Z , the renormalized topological mass \tilde{M} , and renormalized velocity \tilde{v} such that the resulting Green function in the low-energy limit has the form

$$G(\mathbf{k} = \mathbf{K} + \mathbf{q}, \omega) = \frac{Z}{\omega - \tilde{v}\mathbf{q} \cdot \boldsymbol{\sigma} - \tilde{M}\sigma_z}. \quad (\text{S3})$$

Then using Σ_E , Σ_z and Σ_p from $\Sigma(\mathbf{k}, \omega)$ we can express Z , \tilde{M} and \tilde{v} as:

$$Z^{-1} = 1 - \Sigma_E, \quad (\text{S4})$$

$$\tilde{M} - M_i = (M - M_i + \Sigma_z)Z^{-1}, \quad (\text{S5})$$

$$\tilde{v} = v(1 + \Sigma_p/v)Z^{-1}, \quad (\text{S6})$$

To calculate $\Sigma(\mathbf{k}, \omega)$, we treat $V(\mathbf{r})$ perturbatively. In momentum space, V is a delta function connecting \mathbf{k} to $\mathbf{k} \pm Q\hat{x}$ and $\mathbf{k} \pm Q\hat{y}$. Hence, at second order the self energy is

$$\Sigma^{(2)}(\mathbf{k}, \omega) = (W/2)^2 \sum_{\pm, \hat{\mu}=\{\hat{x}, \hat{y}\}} \frac{1}{\omega - h_0(\mathbf{k} \pm Q\hat{\mu})}. \quad (\text{S7})$$

Near $M = 4$, $\mathbf{k} = \mathbf{M} + \mathbf{q}$ with $\mathbf{M} = (\pi, \pi)$, this yields

$$\Sigma_E^{(2)} = -\frac{W^2}{D_2}, \quad (\text{S8})$$

$$\Sigma_p^{(2)} = \frac{W^2}{2} \frac{(4 - M)^2(1 + \cos Q)}{D_2^2} v, \quad (\text{S9})$$

$$\Sigma_z^{(2)} = W^2 \frac{(4 - M) + (\cos Q - 1)}{D_2}, \quad (\text{S10})$$

where $D_2 = (4 - M)^2 + 2(3 - M)(\cos Q - 1)$ is the common denominator that is always positive for $M > 3$. Observe that the numerator of $\Sigma_z^{(2)}$ is also always negative for $M > 4$, and $\Sigma_E^{(2)}$ is always negative. Hence \tilde{M} is renormalized to be smaller as W increases, predicting a critical W where $\tilde{M}(W) = 4$ where TI to CM transition occurs. On the other hand, the direction of velocity renormalization is not obvious from the second-order perturbation theory, and indeed we can only predict the velocity to be renormalized to 0 at fourth-order perturbation theory. This is indicative of scattering off a single Dirac cone, where due to spin selection rules it requires a larger momentum exchange to induce intranode scattering.

The fourth-order perturbation theory includes all of the diagrams that connect the Dirac node to points in the Brillouin zone that are $2Q$ Manhattan distance apart and then back. The fourth order contributions to $\Sigma(\mathbf{k}, \omega)$ are

$$\begin{aligned} \Sigma_E^{(4)} = \frac{W^4}{4} & (-15M^4 + 166M^3 + (-36M^2 + 206M - 295)\cos(3Q) - 732M^2 + \\ & (2M(M(24M - 221) + 697) - 1497)\cos(Q) + (2M(M(13M - 115) + 356) - 770)\cos(2Q) + \\ & 6(M - 3)\cos(4Q) + 1522M - 1260)/D_4 \end{aligned} \quad (\text{S11})$$

$$\begin{aligned} \Sigma_z^{(4)} = \frac{W^4}{8} & (-10M^5 + 138M^4 - 806M^3 + 2509M^2 + (2M(2M(M(11M - 134) + 622) - 2615) + 4212)\cos(Q) + \\ & 2(M(M(3M(3M - 37) + 538) - 1208) + 1048)\cos(2Q) + 2(451 - 6M(M(3M - 26) + 76))\cos(3Q) + \\ & 5(M - 3)(3M - 8)\cos(4Q) - 2(M - 3)\cos(5Q) - 4155M + 2904)/D_4 \end{aligned} \quad (\text{S12})$$

where D_4 is the common denominator

$$\begin{aligned} D_4 = & (-2(M - 3)\cos(Q) + (M - 6)M + 10)^2(-4(M - 2)\cos(Q) + \\ & (M - 4)M + \cos(2Q) + 7)(-2(M - 3)\cos(2Q) + (M - 6)M + 10) \end{aligned} \quad (\text{S13})$$

With the fourth-order correction, we find that the perturbation theory agrees very well with the numerical results as demonstrated in the main text as well as Figs. S1 and S2. However, fourth order perturbation theory for the velocity renormalization only qualitatively predicts the magic-angle transition where $\tilde{v} = 0$, but at a much larger W than indicated by numerical results. It is natural to expect that this is due to the single node nature of the bandstructure at $\mathbf{M} = (\pi, \pi)$ (all of the scattering is intranode). We anticipate a better prediction of magic angle transition may be achievable only at even higher orders of perturbation theory.

Using exactly the same procedure we can consider the case of M near 2, which is the SM line that divides the two TI regions with opposite sign in the quantum spin Hall effect. From a symmetry point of view it is not surprising that the $M = 2$ SM line is W -independent. This is indeed the case from the perturbation theory, as up to fourth

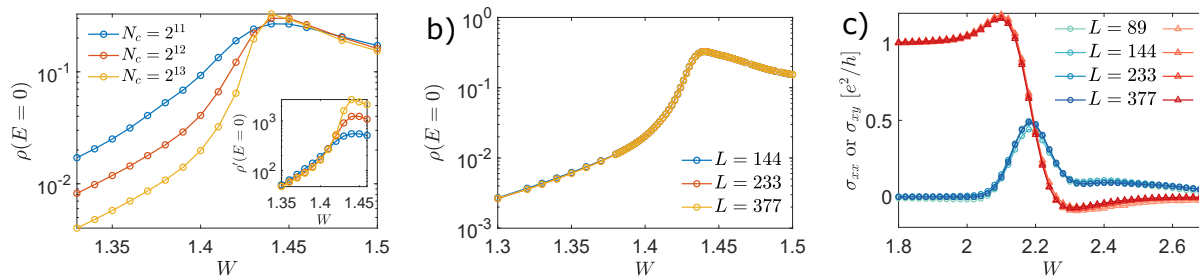


FIG. S5. **Finite size dependence of the density of states and conductivity.** (a) The N_c and (b) L dependence of $\rho(E=0)$ for $M=2$ as a function of W . As the expansion order N_c is increased, the rise of $\rho(E=0, W)$ is much more steep right before the transition. The inset shows $\rho'(E=0)$, computed as $\rho' = N_c \rho$, in the regime this is N_c independent we can extract the renormalized velocity \tilde{v} from this scaling. The L dependence is very weak for $N_c = 2^{13}$. (c) The L dependence of σ_{xy} and σ_{xx} as we fix $N_c = 2^{10}$ for the cut $M = 3.3$. These results demonstrate that we are close to converged in L and the largest finite size effect in the data stems from the finite KPM expansion order.

order we have $\Sigma_z^{(2)} = 0$ and $\tilde{M} = M = 2$, hence there is no topological mass renormalization. That means starting from such a SM phase, quasiperiodicity is not driving it out of SM due to curvature in the phase boundary. At second order the velocity only reduces but does not go to zero and the renormalization of \tilde{v} is only due to the quasiparticle residue $\Sigma_E^{(2)} = -\text{csc}(Q/2)^2$, while $\Sigma_p^{(2)} = 0$. This can be understood as follows, at $M=2$ the two Dirac cones are at $\mathbf{X} = (\pi, 0)$ and $\mathbf{Y} = (0, \pi)$ and being separated by 2π Manhattan distance in momentum space, second order perturbation theory will not be able to induce internode scattering. Whereas, at fourth order the two Dirac cones can be connected by $2Q$ hops in the Brillouin zone. Thus, only fourth order perturbation will be able to predict a vanishing velocity and a magic-angle transition. In line with this reasoning, the renormalized velocity \tilde{v} up to fourth order is

$$\tilde{v} = (v + \Sigma_p^{(2)} + \Sigma_p^{(4)})/Z \quad (\text{S14})$$

Here $\Sigma_p^{(2)}$ vanishes, and the fourth order term

$$\Sigma_p^{(4)} = \frac{W^4}{16^2} (1 + 4 \cos(Q)) \text{csc}(Q/2)^4 v \quad (\text{S15})$$

is negative only when $Q > \cos^{-1}(1/4) \approx 1.82$. Only in this regime does the perturbation theory predict a magic-angle transition. For example, at $Q = 2\pi F_{n-2}/F_n$, it predicts \tilde{v} to vanish at $W_c^{(4)} = 4 \sin(Q/2) (-1 - 4 \cos(Q))^{-1/4} \approx 3.16$. This fourth order perturbative result $W_c^{(4)}$ is an overestimate of the true critical W_c , and thus a more accurate prediction will require higher order perturbation theory. For smaller Q such as $Q = 2\pi F_{n-3}/F_n$, the velocity can never reach 0 at fourth order in perturbation theory. Hence, the magic-angle transition is an even higher order effect than that of $Q = 2\pi F_{n-2}/F_n$. In other words, the reduction of the value of Q requires higher order in perturbation (more Q “hops”) to capture internode scattering.

IV. FINITE SIZE EFFECTS

A. Density of states and conductivity

In this section we discuss the finite size effects in the KPM calculations of the density of states and the conductivity. The numerical calculation puts the model on a lattice with a linear size L , while the truncation of the polynomial expansion at expansion order N_c in the KPM controls the energy resolution. As N_c and L increase (attempting to approach the thermodynamic limit), the observables we calculate using the KPM (i.e., the density of state $\rho(E)$, the resistivity ρ_{xx} , the longitudinal and Hall conductivities σ_{xx} and σ_{xy}) all become sharper, allowing us to accurately determine the critical points.

As an example, we show in detail the N_c and L dependence near the SM-to-CM transition at $M=2$, see Fig. S5(a,b). For fixed $L=233$ and varying N_c , we see that the behavior of the density of states sharpens near the transition, demonstrating that the transition occurs between $W=1.46$ and $W=1.48$. Also we see that at least for density of states at zero energy, taking $L=144$ is adequate for N_c up to 2^{13} , as the $\rho(E=0, W)$ curve does not change at

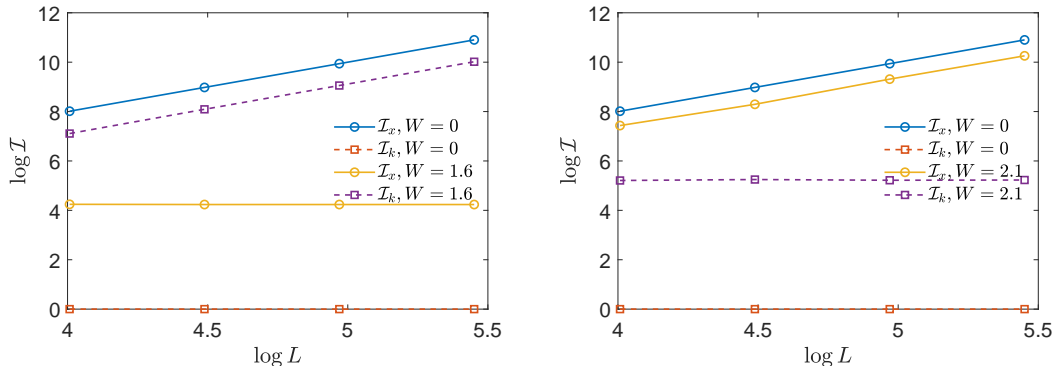


FIG. S6. **L dependence of the IPR** Here we demonstrate two examples of how we determine γ_α for IPR data in the basis $\alpha = x, k$, where $I_\alpha \sim L^{-\gamma_\alpha}$, for $M = 2.7$ (a) and $M = 3.3$ (b). We take a linear fit for $\log I_k$ or $\log I_x$ over $\log L$, then the slope of the fit estimates γ .

all as we vary L above 144. To determine the renormalized velocity \tilde{v} from the density of states we use the scaling of the SM $\rho(E) \sim \tilde{v}^{-2}|E|$ to obtain the scaling with the KPM expansion order $\rho(0) \sim \tilde{v}^{-2}(1/N_c)$. Here, we have used the fact that the infrared low-energy scale (δE) induced by the finite KPM expansion order is related to N_c via $\delta E = \pi D/N_c$ where D is the total bandwidth of the Hamiltonian. As shown in the inset of Fig. S5(a), we find excellent data collapse of $N_c\rho(0)$ that we use to extract \tilde{v} in the SM phase.

In the main text, we have shown examples of the N_c dependence of the conductivity and the resistivity, where a larger cutoff leads to a steeper change in the $\rho_{xx}(W)$ curve near the critical W , and a longer range of W where σ_{xy} is quantized. In Fig. S5(c) we show the L dependence of the longitudinal and Hall conductivities near W_c as we vary L but fix N_c . In this data we see that for $L = 89$ there is a slight variation from the other values of L , but above $L = 144$ the $\sigma_{xx}(W)$ and $\sigma_{xy}(W)$ are not changing at all for the different L 's. Again this justifies the use of $L = 144$ for N_c up to 2^{10} to calculate conductivity as in the main text.

B. Inverse Participation Ratio

The inverse participation ratios (IPR) reflects the structure of the wavefunction in a particular basis and is commonly used to study Anderson localization transitions. When the IPR is independent from system size, the system is localized; when the IPR scales as $1/L^d$ where L^d is the volume of the d -dimensional lattice, the system is extended. When the IPR vanishes with a power law less than d , the wavefunction is critical. To consistently assess the behavior of the IPR, we calculate the IPR (in both real and momentum space bases) for each combination of parameters at $L = 55, 89, 144$ and 233 . Then we fit the log of the IPR $\log(\mathcal{I})$ vs $\log L$, and extract the slope, which is the power law. We demonstrate some examples of such fitting in Fig. S6. The results of the IPR scaling shown in the main text and in Fig. S8 are all computed in this way.

V. EXTRACTING THE SPECTRAL GAP

The size of the insulating gap corresponds to the topological mass \tilde{M} , and for the topological insulator to metal phase transition the power-law scaling of the gap size allows us to extract critical exponents at the TI to CM transition.

To identify the size of the gaps, the most accurate and efficient way we have found is to use the Lanczos algorithm to find lowest energy state in N samples, and then the gap size is the smallest of these individual minima. The smallest energy of each sample is always within $2\pi/L$, the momentum grid spacing, from the true minimum of the band. The lowest eigenvalues from each of the N samples randomly sample this range. The probability to have at least one eigenvalue is less than \mathbf{p} away in momentum space from the true lowest eigenvalue is $1 - (1 - |\mathbf{p}|L/2\pi)^N$. Hence assuming continuity of the dispersion relation, a moderately large L and N can approximate the gap size to very high accuracy. Here, we demonstrate a few examples of the gap size extracted using the Lanczos method with various L . As shown in Fig. S7(a-c) the result is essentially L independent.

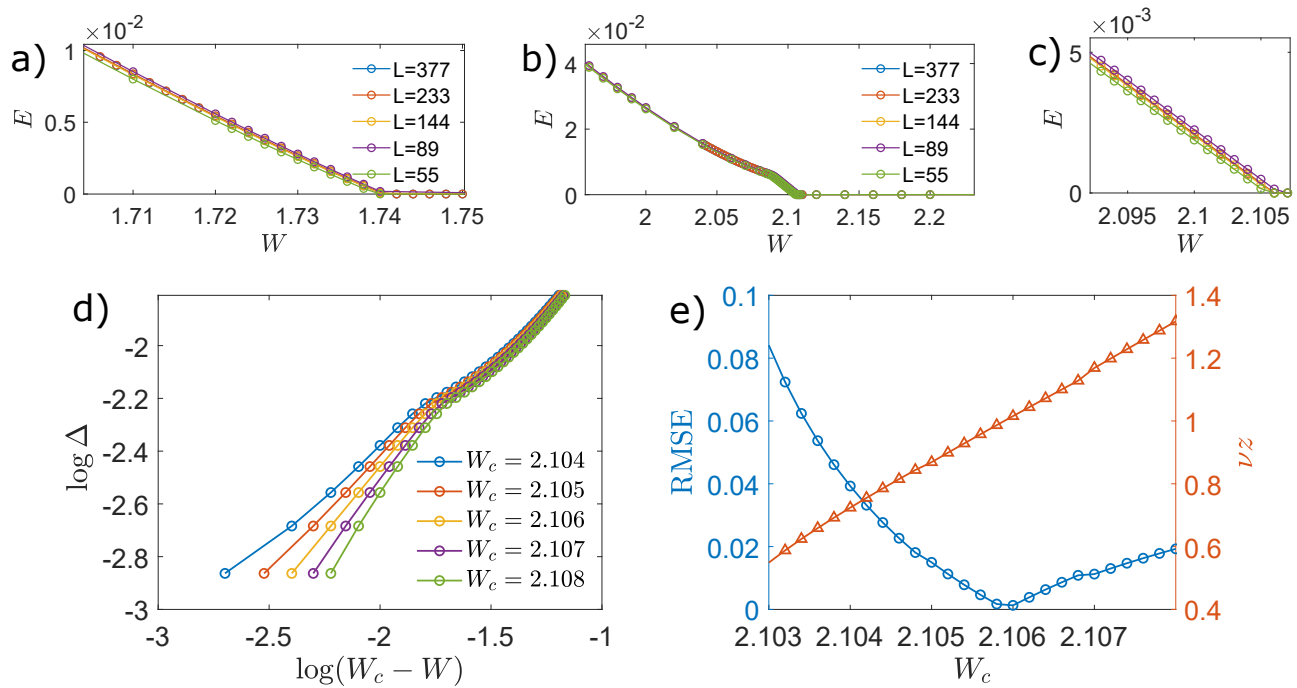


FIG. S7. **Vanishing of the spectral gap.** The gap size as a function of W for $M = 2.4$ (a) and $M = 3.0$ (b) with various system sizes L . (c) is a more zoomed in view of the $M = 3.0$ cut near the transition. In the second row, we show an example of how the combination of critical exponents νz is extracted from the spectral gap data. For a range of choices of W_c , we fit $\log \Delta$ against $\log(W_c - W)$ in the range when $W_c - W$ is under 0.015 and $\Delta > 0.001$ with a straight line. This data is shown in (d). Then we find the point where the root mean square error (RMSE) as shown in (e) of the linear fit is smallest as our best estimation of W_c , where the slope is then νz . For these results, our best estimate of $\nu z = 1.0 \pm 0.1$, with $W_c = 2.106 \pm 0.001$.

A. Critical Exponents at the topological insulator to metal phase transition

The critical exponents at the TI-to-CM phase transition can be extracted from the gap size, as quoted in the main text. Here we demonstrate this process in more detail. We first estimate the critical quasiperiodic strength W_c from the density of states data. Near the estimated W_c , we consider a range of W_c and fit $\log(\Delta)$ over $\log(W_c - W)$ where Δ is the gap size, see Fig. S7(d). Then we identify the range of W that $\log \Delta$ is linear to $\log(W_c - W)$ and use least square fit. The best W_c is picked according to the goodness of linear fit, here quantified with root mean square error of the fit, see Fig. S7(e). The slope of the best fit is then νz , where $\Delta \sim (W_c - W)^{\nu z}$. For some cases this critical exponent is difficult to determine accurately because of the very fine phase diagram structure. For a few fixed M cuts shown in the main text, including $M = 2.4$, $M = 3.0$, $M = 3.3$ and $M = 3.8$, we find νz near 1.0. To be precise, for $M = 2.4$ we have $\nu z = 1.06 \pm 0.1$; for $M = 3.0$, $\nu z = 1.00 \pm 0.1$; for $M = 3.3$, $\nu z = 0.95 \pm 0.2$; for $M = 3.8$, $\nu z = 1.13 \pm 0.15$

B. Gapsizes and IPR

Another interesting feature is the boundary where our perturbation theory works to determine the gap size. The perturbation theory expression of the gap size gives a qualitatively correct prediction of the dependency of Δ on W , but the trend has a turning point at some finite W after which it no longer follows the perturbation theory. This is when the lowest band is no longer clearly the topological band, but mixes with other minibands nearby in energy due to the quasiperiodic potential. We show that the IPR of the lowest energy state changes dramatically at the same W where the gap size turns down as shown in Fig. S8.

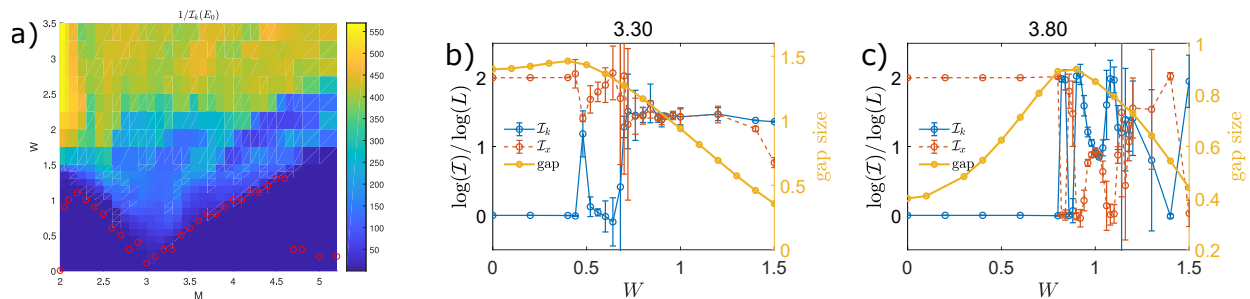


FIG. S8. **Properties of the IPR.** (a) Phase diagram of the momentum space IPR of the lowest eigenstates. The red circles mark where the gap size $\Delta(W)$ changes its trend from increasing to decreasing as determined by the location of the maximum in $\Delta'(W)$. The cuts $M = 3.3$ (b) and $M = 3.8$ (c) show the non-trivial L dependence of the IPR in both real and momentum space start to dramatically change when $\Delta(W)$ begins to turn downward.

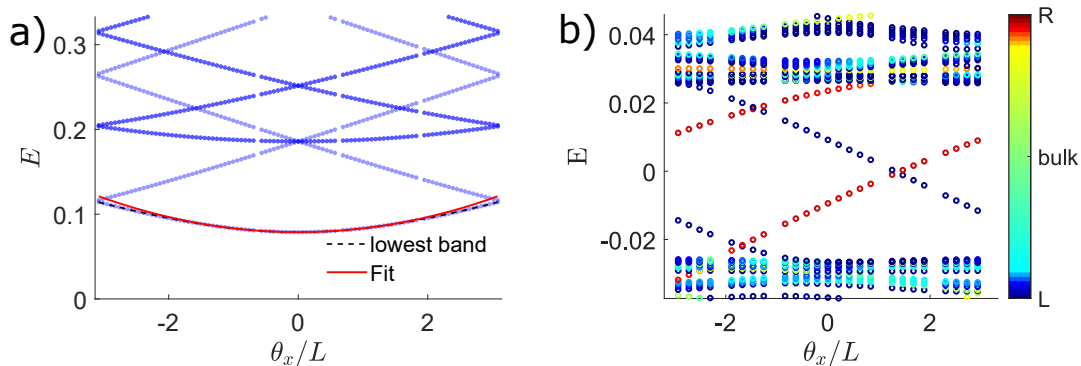


FIG. S9. **Twist Dispersions.** (a) Using the twist dispersion to obtain the effective mass m^* . The red curve is the quadratic fitting result to estimate m^* . (b) Twist dispersion with open boundary conditions in the y direction and twisted boundary conditions in the x direction. The color corresponds to the location of the eigenstates along the y axis. The red and dark blue states in the bulk gap are the edge states.

VI. DISPERSION RELATION AND EFFECTIVE MASS

In this section, we discuss the twist dispersion from which we check for topological edge states and obtain the effective mass. The twisted boundary condition we implemented, $t_\mu \rightarrow t_\mu e^{i\theta_\mu/L}$, effectively momentum \mathbf{k} by $\boldsymbol{\theta}/L$ (in the limit of $W = 0$). Hence the dispersion relation $E(\mathbf{k})$ projected onto $1/L$ th of the Brillouin zone can be computed through $E(\boldsymbol{\theta})$. Then the effective mass is obtained by fitting the dispersion relation near the minimum with a quadratic function as shown in Figure S9(a), for example.

A. Edge states

For finite size calculation, (twisted) periodic boundary condition eliminates all edge contribution and keeps only the bulk. With open boundary conditions the edge states can be observed. Here, we use twisted boundary conditions only on the x direction but keep the boundary open along the y direction, so that we can see the dispersion of the edge states, as clearly demonstrated in Fig. S9.

[S1] T. Ohtsuki and T. Ohtsuki, Journal of the Physical Society of Japan **85**, 123706 (2016).

[S2] J. Carrasquilla and R. G. Melko, Nature Physics **13**, 431 (2017).

[S3] P. Baldi, P. Sadowski, and D. Whiteson, Nature communications **5**, 4308 (2014).

[S4] A. Krizhevsky, I. Sutskever, and G. E. Hinton, in *Advances in neural information processing systems* (2012) pp. 1097–1105.

- [S5] C. M. Bishop, *Pattern recognition and machine learning* (springer, 2006).
- [S6] G. E. Hinton, N. Srivastava, A. Krizhevsky, I. Sutskever, and R. R. Salakhutdinov, arXiv preprint arXiv:1207.0580 (2012).